Journal of Alloys and Compounds 853 (2021) 157329

Contents lists available at ScienceDirect

Journal of Alloys and Compounds

journal homepage: http://www.elsevier.com/locate/jalcom

Prussian Blue modified Metal Organic Frameworks for imaging guided synergetic tumor therapy with hypoxia modulation

Haiqing Gao [a, 1], Bin Chi [b, c, 1], Feng Tian [a], Mingyue Xu [a], Zushun Xu [a], Ling Li [a, *], Jing Wang [b, c, **]

[a] Ministry-of-Education Key Laboratory for the Synthesis and Application of Organic Function Molecules, Hubei Collaborative Innovation Center for Advanced Organic Chemical Materials, Hubei University, 430062, China
[b] Department of Radiology, Union Hospital, Tongji Medical College, Huazhong University of Science and Technology, Wuhan, 430022, China
[c] Hubei Province Key Laboratory of Molecular Imaging, Wuhan, 430022, China

ARTICLE INFO

Article history:
Received 25 July 2020
Received in revised form
22 September 2020
Accepted 23 September 2020
Available online 28 September 2020

Keywords:
Nanostructures
Surfaces and interfaces
Nanofabrications
pH-responsive
PTT
CDT

ABSTRACT

In this study, a hybrid material UIO-66-NH_2/PB were synthesized through the modification of Prussian Blue on the surface of Metal Organic Frameworks for synergetic tumor therapy with hypoxia modulation. It was found that UIO-66-NH_2/PB has good photo-thermal performance and photo-thermal stability, suitable for photo-thermal treatment. Dissolved oxygen analysis showed that UIO-66-NH_2/PB can catalyze H_2O_2 into O_2. It was proved that this process is accompanied by the generation of ·OH. Furthermore, with the irradiation of 808 nm for 5min, the TMB solution becomes darker blue, proving that more free radicals are produced. The produced O_2 can be used to modulate the hypoxia of tumor to improve the anti-cancer efficiency, and the generated ·OH can kill cancer cells to achieve chemo-dynamic therapy. Doxorubicin (DOX) was selected as a model drug and the DOX loading of UIO-66-NH_2/PB was 67%. Drug release experiments showed that DOX was not nearly released in pH 7.4, while 78% DOX was released in pH5.8 after 40 h, demonstrating the excellent pH-responsive release. In addition, with the irradiation of 808 nm for 5min, 87% DOX was released in pH 5.8, indicating photo-thermal effect could help achieve better release effect. The different cytotoxicity to L-02 cells and HeLa cells of UIO-66-NH_2/PB shows UIO-66-NH_2/PB is only harmful to cancer cells, indicating that Fenton-like reaction only occurred in tumor to generate ·OH. *In vivo* experiment showed synergetic therapy can achieve satisfactory treatment efficiency. Therefore, UIO-66-NH_2/PB is expected to combine multiple treatments to improve anti-cancer effect.

1. Introduction

According to the GLOBOCAN, approximately 18 million cancer cases were newly diagnosed and about 9 million people died from cancer in 2018 [1]. Therefore, how to improve the treatment efficiency of cancer has been a focused research direction. In recent years, kinds of cancer therapies, have been explored in clinical trials to inhibit tumor proliferation and prolong the survival of patients, including chemotherapy, radiotherapy, photodynamic therapy (PDT), immunotherapy, chemo-dynamic therapy (CDT) and photo-thermal therapy (PTT) [2–4]. Among these, chemotherapy is still most widely used in cancer treatments. However, conventional chemotherapy has a low bioavailability and can generate non-specific drug accumulation, which can cause side effects [5]. Therefore, designing a smart carrier to reduce side effects is essential. In recent years, stimuli-responsive materials have gradually become popular because of their time-space controllable properties, which provide a choice for the design of controllable drug delivery systems [6].

Metal–organic frameworks (MOFs), as a porous material, with high drug-loading capacity, good biodegradability, good biocompatibility and easy functionalization, have been widely investigated for intelligent drug delivery in recent years [7–11]. Among the MOF nanocarriers triggered by multiple stimuli (pH, redox, temperature and light, ect), due to the acidic tumor microenvironment (TME), which is sensitive to the coordination bonds between MOFs and

* Corresponding author.
** Corresponding author. Hubei Province Key Laboratory of Molecular Imaging, Wuhan, 430022, China
E-mail addresses: lingli@hubu.edu.cn (L. Li), jjwinflower@126.com (J. Wang).
[1] These authors contributed equally to this work.

https://doi.org/10.1016/j.jallcom.2020.157329
0925-8388/

drug molecule, the pH-responsive MOFs are the most widely investigated [6]. Many pH-responsive MOFs have been reported for drug delivery [12–14]. For example, FA-PEG decorated MOF(FA-PEG/CQ@ZIF-8) is used for pH-responsive release of CQ [15], Succinylated-Zein-ZIF-8 for pH-responsive drug delivery [16], Zn-MOF-74 for pH-responsive delivery As_2O_3 [17], ect. UIO-66-NH_2 (Zr-MOF) can be used for drug delivery, and can release anticancer drugs through pH response to reduce the toxic and side effects on normal cells [18]. However, long-term use of the same drug is prone to multidrug resistance (MDR) and reduces the efficiency of chemotherapy [5].

Hypoxia, one of the characteristics of TME, is considered as a direct cause of multidrug resistance [19–21]. It was found that both tumor recurrence and metastasis are characterized by hypoxia [22]. Therefore, to overcome the limited supply of oxygen in tumors can help improve the treatment efficiency of therapy. Tumor cells have the ability to grow indefinitely, proliferate, new blood vessels, and invade and metastasize, which is closely related to the production of H_2O_2, causing H_2O_2 levels in cancer cells to be much higher than normal cells. Taking advantage of rich H_2O_2 in tumors, O_2 can be generated through catalytic reactions to regulate the hypoxic environment.

With the introduction of the new concept of "Nanocatalytic Medicine" (NCM) in 2018 [23], overexpressed H_2O_2 in cancer cells was used to produce O_2 through Fenton reaction to regulate TME, accompanied by generation of ·OH to kill cancer cells and further improve the treatment efficiency [19]. Increasing researchers began to pay attention to chemo-dynamic therapy (CDT) based on Fenton reaction and integrate it into drug carrier. Recently, Chowdhuri et al. have synthesized a self-reinforcing CDT nanoagent based on MnO_2, with Fenton-like Mn^{2+} delivery and glutathione (GSH) depletion properties. And successfully achieve MRI-monitored chemo-chemo-dynamic combination therapy [24]. Wang et al. also designed biomimetic CS-GOD@CM nano-catalysts, composed of ultra-small $Cu_{2-x}Se$(CS) nanoparticles, glucose oxidase (GOD), and tumor cell membrane (CM), in conjunction with the NIR-II irradiation, which significantly enhanced the kinetics of Fenton reaction for CDT treatment of breast cancer [25].

However, Fenton reaction generally needs to be performed in pH 2.5–4.5. In the weak acidic environment of tumors (pH 5.8), the rate of Fenton reaction is slow, impairing the efficiency of chemo-dynamic therapy. Therefore, it is need to speed up the rate of Fenton reaction in tumor cells.

Prussian blue (PB), with the ideal formula of $Fe^{III}_4[Fe^{II}(CN)_6]_3 \cdot nH_2O$, is considered to be a promising photothermal material for theranostics in biomedical field due to its special structure [26]. In this structure, Fe^{3+} are connected to nitrogen atoms of cyanides, and Fe^{2+} are linked by carbon atoms of cyanides, forming a cubic crystal [27]. It has been approved by the US FDA for photothermal therapy (PTT) [4,28,29]. Therefore, several nanoparticles based on PB were prepared for photo-thermal therapy [26,28]. Furthermore, the unique structure of PB also gives it excellent performance in magnetic resonance imaging and fluorescence imaging, providing the basis for bioimaging [30–32], which can provide detailed information about cancer cells to achieve imaging guided therapy. However, the Fenton-like reaction performance of PB is rarely reported. In fact, PB can be oxidized by H_2O_2 to Berlin Green (BG), while releasing hydroxyl radicals (•OH) [33,34].

$$KFe^{(III)}Fe^{(II)}(CN)_6 + H_2O_2 \rightarrow K^+ + Fe^{(III)}Fe^{(III)}(CN)_6 + \cdot OH + OH^-$$

(PB) (BG)

Berlin green energy oxidizes H_2O_2 to emit O_2:

$$K^+ + Fe^{(III)}Fe^{(III)}(CN)_6 + H_2O_2 \rightarrow KFe^{(III)}Fe^{(II)}(CN)_6 + H_2O + 1/2\ O_2$$

(BG) (PB)

PB/BG continuously generates •OH and O_2. The produced oxygen from PB can increase the oxygen concentration of hypoxia of tumor cells and reduce drug resistance, and the generated •OH can induce cancer cell death through oxidative damage of lipids, proteins and DNA [3]. On the other hand, after PB gains energy, electron transfer occurs internally, accelerating the generation of •OH and O_2. Therefore, combining the photo-thermal performance of PB and the Fenton-like catalytic performance, it is possible to accelerate the Fenton reaction rate by using photo-thermal effect. Combined with the photo-thermal effect of PB, PB can convert the near-infrared light into heat to accelerate the rate of Fenton reaction, producing more • OH to kill more cancer cells.

Considering the complexity, heterogeneity and diversity of tumor, combination therapy employing two or more therapeutic strategies can hopefully elevate the mono-therapeutic effects in treatment [35]. Inspired by this, we attempt to develop an intelligent drug carrier by growing PB on the surface of UIO-66-NH_2. UIO-66-NH_2/PB has been proposed for imaging guided synergetic therapy of chemotherapy, photo-thermal therapy and chemo-dynamic therapy (Scheme 1). This hybrid material also can load anticancer drug DOX with a high drug loading rate of 67%. More importantly, the as-prepared UIO-66-NH_2/PB can release loaded DOX in acidic environments, demonstrating the excellent pH-responsive release. Simultaneously, photo-thermal effect could help release more DOX. With near-infrared light irradiating 10 min, its temperature can increase over to 54 °C, which exceeds the limit temperature for the survival of cancer cells [4]. Dissolved oxygen analysis shows that UIO-66-NH_2/PB can catalyze H_2O_2 into O_2, and this process is accompanied by the generation of •OH, which is proved by the experiment phenomena that the solution of 3,3′,5,5′-tetramethylbenzidine (TMB) turns blue. Furthermore, with the irradiation of 808 nm for 5min, the TMB solution becomes darker blue, proving that more free radicals are produced. The produced O_2 can be used to modulate the hypoxia of tumor to reduce resistance. The different cytotoxicity to L-02 cells and HeLa cells of UIO-66-NH_2/PB shows UIO-66-NH_2/PB is only harmful to cancer cells. The reason is that Fenton-like reaction can only occur in acid environment of tumor and generate •OH. As a result, DOX loaded UIO-66-NH_2/PB can achieve synergetic tumor therapy with hypoxia modulation, achieving a satisfactory treatment effect.

2. Experimental

2.1. Materials and instruments

Potassium ferricyanide, Zirconium chloride (IV), 2-amino-terephthalic acid, polyvinylpyrrolidone (PVP) and doxorubicin (DOX) were all purchased from Aladdin Industrial Corporation (Shanghai, China). Reagents and solvents were of analytical reagent grade and used without further purification. Fresh double distilled water was used throughout the experiment.

The power X-ray diffraction (XRD) measurements were performed using a D8 Advance X-ray diffractometer (Bruker Company, USA). Scanning electron microscope (SEM) images were obtained through a JSM6510LV scanning electron microscope (JEOL, Japan). Transmission electron microscope (TME) images were obtained using a H7500 transmission electron microscope (Hitachi, Japan). Fourier transform infrared (FT-IR) spectroscopy was carried out on a Single frequency infrared spectrophotometer (PerkinElmer, USA).

2.2. Synthesis methods

The detailed synthesis methods were listed in the ESI.

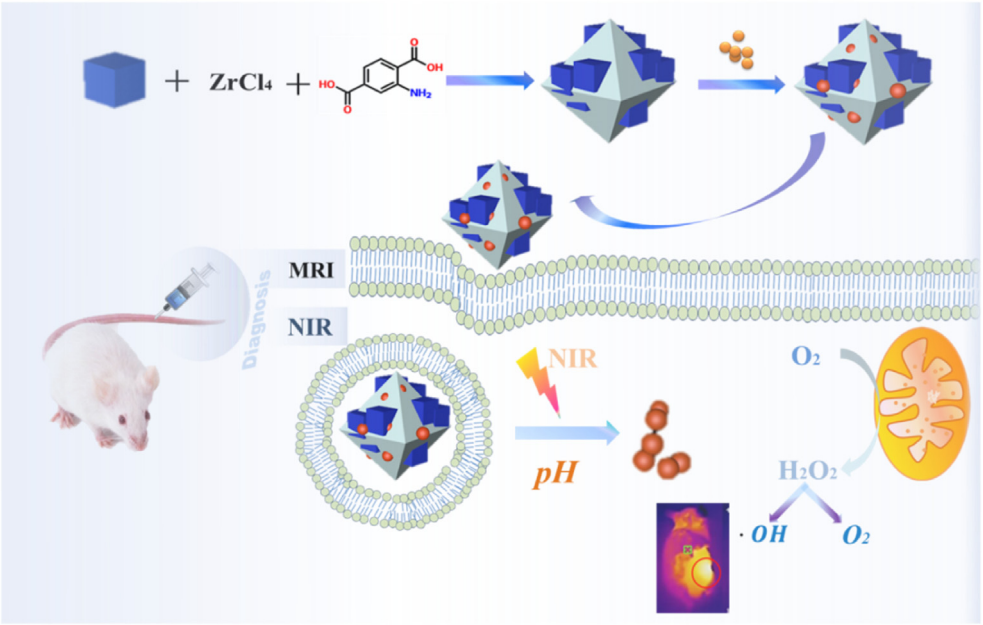

Scheme 1. The synthetic of UIO-66-NH_2/PB and the theory of UIO-66-NH_2/PB particles as a dual-mode imaging and dual-responsive drug carrier for synergistic cancer treatment.

2.3. Drug loading and drug release

The detailed drug loading and drug release methods were listed in the ESI.

2.4. Measurements of photo-thermal property

PB and UIO-66-NH_2/PB aqueous solutions (0, 0.02, 0.05, and 0.2 mg/mL) were irradiated with an 808 nm laser (2.0 W/cm^2) for 10 min. The temperature variation was recorded with a digital thermistor temperature sensor. Besides, thermographs of different solutions were recorded with an infrared thermal camera.

2.5. In vitro cellular toxicity tests

HeLa cell line (Human cervical carcinoma) was grown in DMEM medium supplemented with 10% FBS and 1% penicillin/streptomycin in an incubator with a humidified air atmosphere of 5% CO_2 at 37 °C. The HeLa cells (5×10^3 cells/well) were seeded onto 96-well plates. After 24 h of incubation, cells were treated with the corresponding concentration of UIO-66-NH_2/PB. Complete DMEM medium was used as a blank. Four hours prior to the assay, MTT reagent (20 μL/well, 5 mg/mL) was added to cells. We replaced the medium with DMSO (200 μL/well), and then we read the absorbance at 492 nm by a microplate reader.

2.6. Dissolved oxygen experiment

Use a dissolved oxygen meter to measure the dissolved oxygen content of the hydrogen peroxide solution at pH 5.8 and 7.4. Weigh two 10 mg UIO-66-NH_2/PB, two 10 mg UIO-66-NH_2, add one UIO-66-NH_2/PB and one UIO-66-NH_2 to the pH = 5.8 hydrogen peroxide solution. The other materials were put into a hydrogen peroxide solution of pH = 7.4, respectively. The amount of dissolved oxygen in the hydrogen peroxide solution of pH = 5.8 and pH = 7.4 was measured every 1 min.

2.7. ·OH generation by UIO-66-NH_2/PB-mediated Fenton-like reaction

The generation of ·OH was observed using 3,3′,5,5′-tetramethylbenzidine (TMB). Dissolve 0.03 g TMB in a citric acid solution with pH 4.0 TMB solution, H_2O_2 solution and UIO-66-NH_2/PB solution were added in the centrifuge tube in turn. Observe and record color changes.

2.8. In vivo MRI imaging

The detailed *vivo* MRI were listed in the ESI.

2.9. Mouse tumor model

The tumor-bearing mices were randomly divided into 3 groups (n = 3 each group) when the tumor volume reached about 50 mm^3, including (1) PBS, (2) UIO-66-NH_2/PB, (3) UIO-66-NH_2/PB + NIR. On the first day, the mice were intravenously injected with 150 μL (0.5 mg/mL) UIO-66-NH_2/PB, and the tumor site was irradiated with infrared light. Changes in tumor volume and body weight of mice were recorded.

3. Results and discussion

3.1. Characterization

The crystalline structures of UIO-66-NH_2/PB are affirmed and compared with PB and UIO-66-NH_2 by X-ray diffraction analysis, as shown in Fig. 1a. The characteristic diffraction peaks of PB appear at positions where 2θ is 17°, 24.5°, 36.5°, and 40°, respectively. The peaks at 2θ ° between 10° and 70° are typical intense reflections of UIO-66-NH_2. Compared with PB and UIO-66-NH_2, there are two new peaks of 2θ ° = 12°, 13°, indicating that UIO-66-NH_2/PB is a new material rather than simple mix of UIO-66-NH_2 and PB. Doped with PB, the incident X-rays during the XRD test are slightly shielded, resulting in the XRD peak of UIO-66-NH_2/PB being weaker than that of pure UIO-66-NH_2 [36]The intense peak at 25.7°

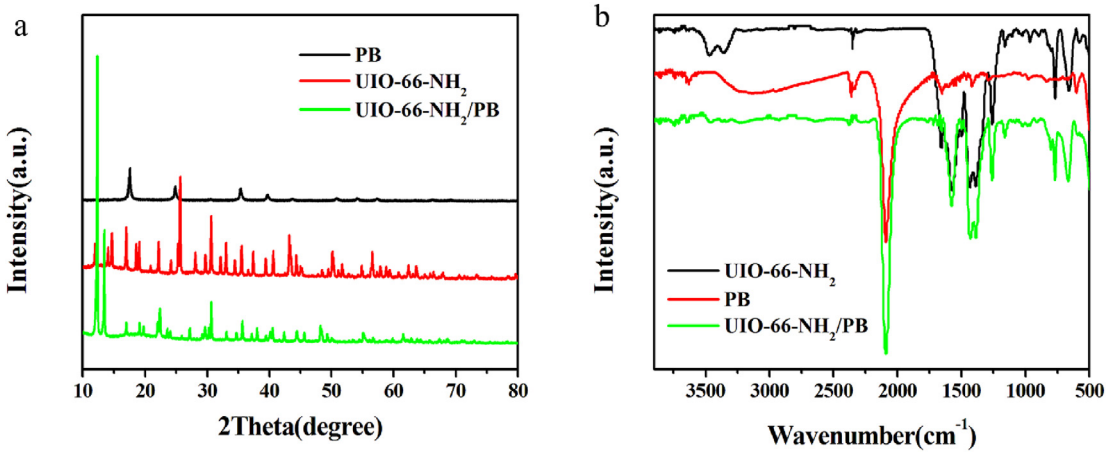

Fig. 1. a) X-ray diffraction (XRD) patterns and FT-IR spectra of PB. b) UIO-66-NH_2 and UIO-66-NH_2/PB.

in UIO-66-NH_2 that corresponds to the crystal plane (224) [37] disappears in UIO-66-NH_2/PB, which may be explained by the coordination between PB and UIO-66-NH_2 affects the crystal plane (224).

The confirmation of UIO-66-NH_2/PB can be further proved by FT-IR, as shown in Fig. 1b. There are two characteristic peaks near 3466 cm^{-1} and 3354 cm^{-1}, which are due to the stretching vibration of the amino functional group on the surface of UIO-66-NH_2. The three peaks appearing between 800 cm^{-1} and 1500 cm^{-1} belong to the benzene ring, and the peak at 1654 cm^{-1} is attributed to the stretching vibration of the carboxyl functional group in the ligand 2-NH_2-BDC. The infrared spectrum of PB has a characteristic peak at 2217 cm^{-1}, which is attributed to the tensile vibration of the cyano functional group in PB. In comparison, the characteristic peaks of UIO-66-NH_2 at 3466 cm^{-1} and 3354 cm^{-1} decrease significantly in UIO-66-NH_2/PB, and the characteristic peak of PB at 3120 cm^{-1} is close to disappearing. It further proves that it is not a simple mix of UIO-66-NH_2 and PB, but a new kind of composite material. In order to be able to observe the changes in some specific portions of the spectra more clearly, we will further magnify the spectrum in the range of 3900 cm^{-1} to 2500 cm^{-1}, as shown in Fig. S1. The change in the spectrum can be explained by the coordination between the Fe ions in PB and the amino group in UIO-66-NH_2.

From TEM images of UIO-66-NH_2, it shows that the particles are well dispersed with uniform in size of 180 ± 10 nm, which is accordance with the SEM images. Fig. 2e shows PB particles have uniform cubic shape with a particle size of 70 ± 5 nm. The image of UIO-66-NH_2/PB (Fig. 2f) shows that PB particles are coated with the surface of UIO-66-NH_2.

The confirmation of UIO-66-NH_2/PB can also be proved by EDX analysis, as shown in Fig. S3. It can be observed that UIO-66-NH_2/PB materials include C, N, O, Zr, Fe elements and the PB attached to UIO-66-NH_2, it is verified that we successfully synthesized hybrid material (UIO-66-NH_2/PB).

Surface morphology of the UIO-66-NH_2, PB, UIO-66-NH_2/PB were examined by SEM, as shown in Fig. 2. All these three kinds of particles are well dispersed, but they are different in size and shape. The PB particles are much smaller than UIO-66-NH_2 particles, and the surface of UIO-66-NH_2/PB particles is not as smooth as that of PB and UIO-66-NH_2. The sizes of UIO-66-NH_2, PB, UIO-66-NH_2/PB are approximately 180 nm, 70 nm and 200 nm, respectively.

The confirmation of UIO-66-NH_2/PB can be further proved by nitrogen adsorption-desorption isotherms, as shown in Fig. S2. From the pore distribution (The inserts of Fig. S2), obvious mesoporous distribution can be both observed at about 30 nm in PB in UIO-66-NH_2 and UIO-66-NH_2/PB. It can be concluded that PB particles can be only attached on the surface of UIO-66-NH_2, without the change of size distribution. This conclusion can be supported by the size of PB particles from SEM images (Fig. 2b). PB particles have uniform cubic shape with a particle size of 70 ± 5 nm, which can hardly be loaded in the pores of UIO-66-NH_2. Therefore, the formation of UIO-66-NH_2/PB depends on the interaction between PB and functional groups on the surface of UIO-66-NH_2. The specific surface area of UIO-66-NH_2 is determined to be 569.595 m^2/g, and specific surface area of UIO-66-NH_2/PB is determined to be 464.478 m^2/g. It further proves that the PB particles are only attached on the surface of UIO-66-NH_2, thus reducing a small part of the specific surface area.

3.2. Photo-thermal analysis

The photo-thermal effect of Prussian blue (PB) is examined, as shown in Fig. 3. Fig. 3a demonstrates the heating curves of PB solutions with different concentrations (0, 0.02, 0.05, 0.2 mg/mL) under near infrared light irradiation (808 nm 2.0 W/cm^2). After 10 min of laser irradiation, the temperature of deionized water increases by only 5 °C; while the temperatures of PB aqueous suspensions at 0.02 mg/mL, 0.05 mg/mL and 0.20 mg/mL concentration increase by about 34 °C, 37 °C and 49 °C, respectively. The results show that with the increase of concentration and laser irradiation time, Prussian blue has better photo-thermal performance. The infrared thermal images of PB within NIR irradiation for 10 min are shown in Fig. 3b.

On basis of the photo-thermal properties of PB, it is believed that UIO-66-NH_2/PB can be also with excellent photo-thermal performance. Heating curves of UIO-66-NH_2/PB solutions with different concentrations (0, 0.02, 0.05, 0.2 mg/mL) under near infrared light irradiation (808 nm 2.0 W/cm^2) are shown in Fig. 3c. The temperature of UIO-66-NH_2/PB solutions climbs up with increasing concentration and laser irradiation time. The temperature of 0.20 mg/mL UIO-66-NH_2/PB solutions reaches 54 °C in 10 min, exceeding the temperature limit for cancer cell survival (>42 °C) [4]. It indicates that UIO-66-NH_2/PB can hopefully be used in photothermal therapy. In order to discuss the thermal stability of UIO-66-NH_2/PB, the photo-thermal cycle experiments of 0.20 mg/mL UIO-66-NH_2/PB solution are performed and the result is shown in Fig. 3d. With Near-infrared irradiation for 5 min, the solution temperature rises to 45 °C, and the solution temperature falls to 24 °C after 5 min of natural cooling. After 5 cycles, the temperature

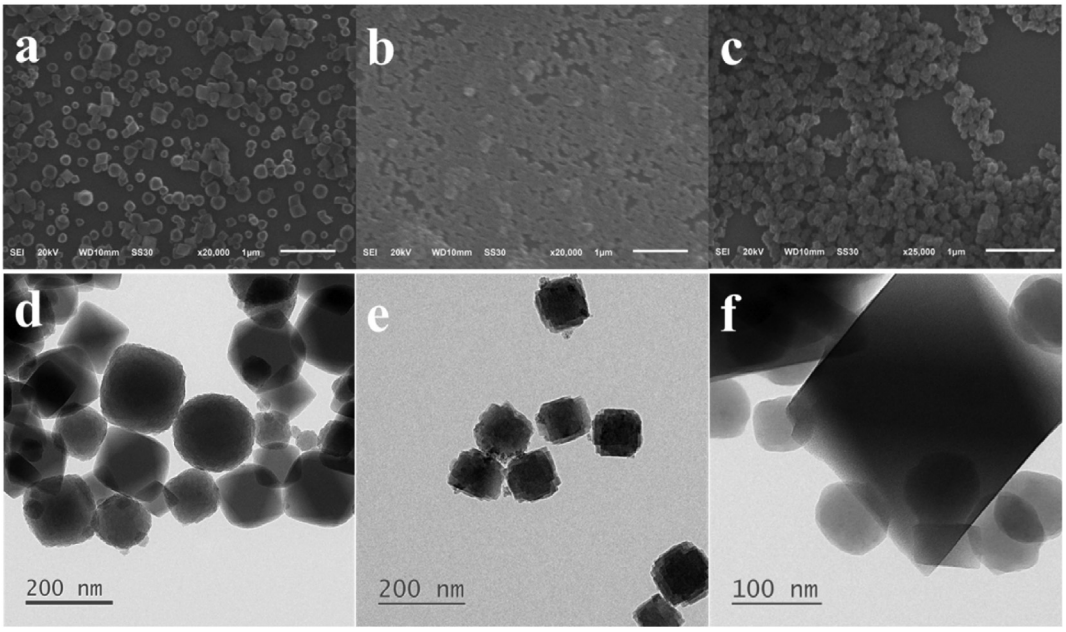

Fig. 2. SEM images of a) UIO-66-NH_2, b) PB and c) UIO-66-NH_2/PB; TEM images of d) UIO-66-NH_2, e) PB and f) UIO-66-NH_2/PB.

can still rise to 45 °C and naturally falls to 25 °C. It proves that UIO-66-NH_2/PB has excellent photo-thermal stability. In addition, we calculated the photo-thermal conversion efficiency of the UIO-66-NH_2/PB, as shown in Fig. S4. The conversion efficiency is 51.5%, shows that the material has good photo-thermal performance.

3.3. Drug loading and drug release

In order to investigate the possibility of UIO-66-NH_2/PB as drug carrier, DOX is selected as drug model to discuss the drug loading and drug release, and the result is as shown in Fig. 4. It is clear that the DOX loading climbs with increasing time. The drug loading of UIO-66-NH_2/PB (after 3 days) was 67.4%, which is much more than that of reported materials. This demonstrates that UIO-66-NH_2/PB has a high drug loading capacity.

In order to explore the stability of UIO-66-NH_2/PB, the X-ray diffraction (XRD) patterns and infrared spectrum of UIO-66-NH_2/PB before and after DOX loading are compared, as shown in Fig. S5. The characteristic diffraction peaks position of the DOX loaded UIO-66-NH_2/PB don't change significantly. This result indicates that the structure of UIO-66-NH_2/PB remain stable after DOX loading. The DOX-loaded UIO-66-NH_2/PB has a new characteristic diffraction peak at 3356 cm^{-1}, which results from the stretching and vibration of the hydroxyl functional group of DOX. The peak at 1654 cm^{-1} which is attributed to the stretching vibration of the carboxyl functional group in the ligand 2-NH_2-BDC decreases clearly after DOX loading. These indicate DOX are loaded in UIO-66-NH_2/PB mainly through the hydrogen bonding between the carboxyl group and hydroxyl functional group of DOX.

In addition, heating curves of 0.20 mg/mL PB, UIO-66-NH_2/PB and UIO-66-NH_2/PB-DOX solutions are compared, as shown in Fig. S6. It can be observed that the temperature rise of UIO-66-NH_2/PB is similar to that of UIO-66-NH_2/PB-DOX, indicating that the photo-thermal performance is not affected after DOX loading. It proves the stability of UIO-66-NH_2/PB.

The pH of cells in the TME (pH~5.8) is lower than that of normal cells (pH~7.4). In order to discuss the pH-responsive release of UIO-66-NH_2/PB, the drug release under different conditions is shown in Fig. 4b. At pH 7.4, DOX is nearly not released, and only about 2% DOX is released after 60 h. It indicates that DOX will be not released in normal cells, thus reducing side effect to normal cells. At pH 5.8, DOX is release fast in the first 12 h and about 47% DOX is released. After 60 h, DOX release reaches the maximum 80%.

In order to assess the stability of UIO-66-NH_2/PB during drug release at pH 5.8, the concentrations of iron ion and zirconium ion were determined through ICP analysis. After UIO-66-NH_2/PB was immersed in pH 5.8 buffer for 4h, the concentration of iron ion was determined to be 9.4 μg/mL and the concentration of zirconium ion was determined to be 4.7 μg/mL. It proves UIO-66-NH_2/PB is not prone to leaking ions, indicating the stability during drug release.

Compared with the reported pH responsive materials recently (Table S1), the values (78%) are beyond average level. The result demonstrates the excellent pH responsive release. This can be explained by the hydrogen bond formed between the hydroxyl groups of DOX and UIO-66-NH_2/PB. With the protonation of hydroxyl groups under acidic conditions, the hydrogen bond dissociates, thus releasing the drug DOX, as shown in Fig. S7.

In order to investigate the effect of near-infrared light on drug release, DOX release experiment at pH is performed with near-infrared light irradiation, as shown in Fig. 4b and Fig. S8. It is clear that 70% DOX is released in the first 12 h and about 90% DOX is released after 60 h. These results show that photo-thermal effect can promote drug release and achieve better drug release, which is expected to enhance anti-cancer effects by increasing DOX concentration in cancer cells.

3.4. Cytotoxicity study

Santos et al. [38] have studied the toxicity of magnolol@UIO-66(Zr). Gross necropsy revealed no signs of macroscopic damage on both livers and kidneys of the test animals. Histopathological evaluation of liver and kidney tissue sections was carried out. The observed granularity and hepatic cytoplasmic swelling were within the limit, and no pathological damage was observed on the glomerulus and proximal tubular epithelium. Prussian blue (PB) nanoparticles are certified for clinical use by the US FDA, and widely

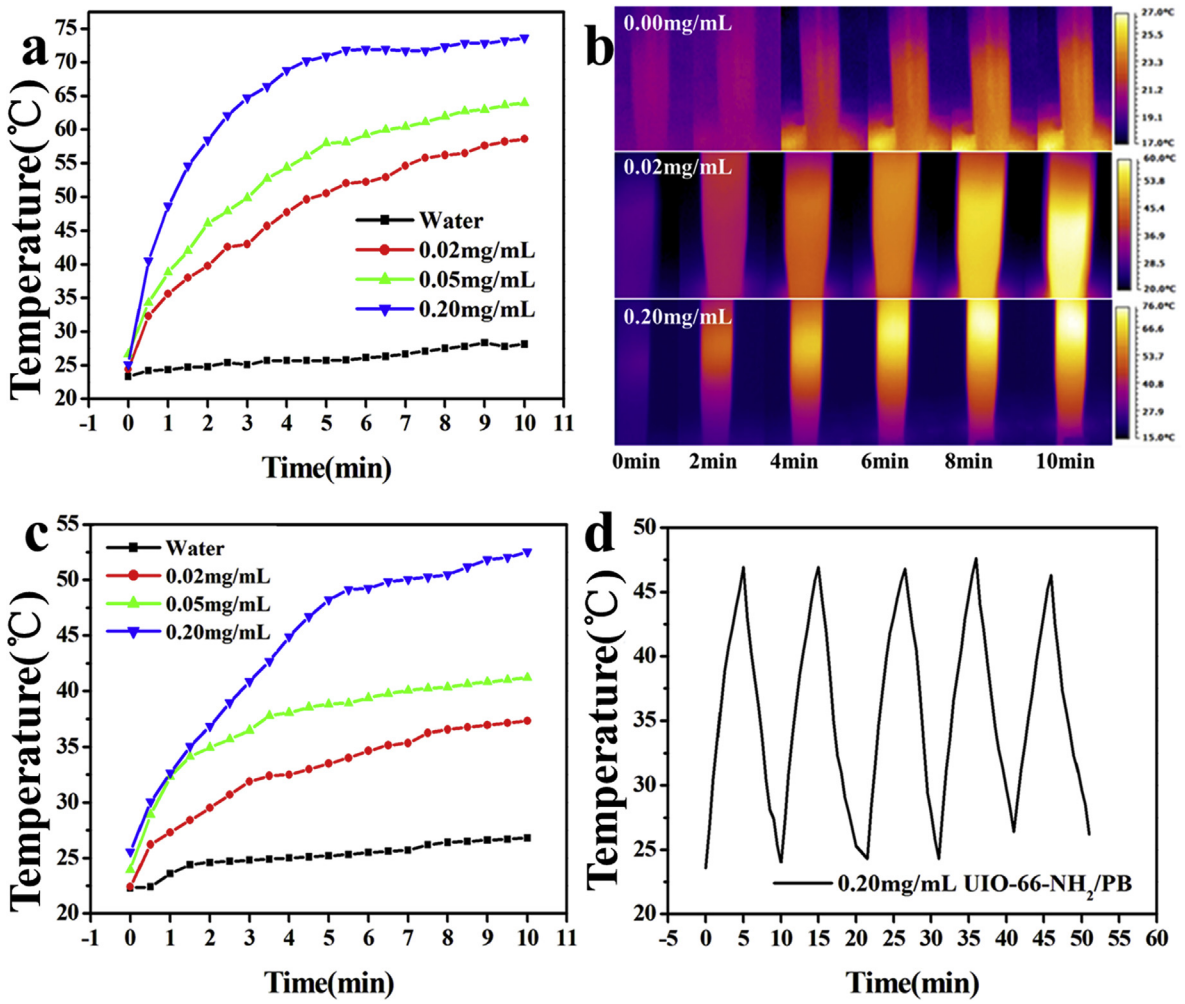

Fig. 3. a) Heating curves of PB solutions of different mass concentrations (0, 0.02, 0.05, 0.2 mg/mL) under 808 nm laser at the power density of 2.0 W/cm^2; b) Infrared thermal images of PB acquired within 10 min NIR irradiation. c) Heating curves of UIO-66-NH_2/PB solutions of different mass concentrations (0, 0.02,0.05, 0.20 mg/mL) under 808 nm laser irradiation at the power density of 2.0 W/cm^2; d) Thermal cycle diagram of 0.20 mg/mL UIO-66-NH_2/PB solution under 808 nm laser irradiation at the power density of 2.0 W/cm^2.

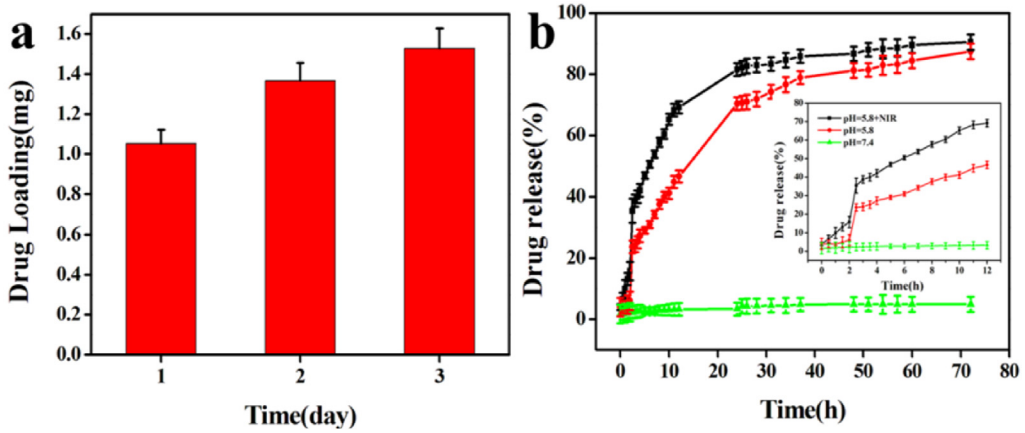

Fig. 4. a) UIO-66-NH_2/PB drug loading on different days; b) DOX release profiles from UIO-66-NH_2/PB under different pH value and near infrared light (NIR). The error bar is the standard deviation of experimental data for three times.

developed as photo-thermal ablation agents [39]. Therefore, it can be concluded that there is no pathological damage of the composite UIO-66-NH_2/PB. To investigate the intracellular microenvironment-targeted drug release of UIO-66-NH_2/PB, cytotoxicity experiments are performed, and the results are shown in Fig. 5. HeLa cells (Human cervical carcinoma) and L-02 cells (hepatocyte cells) represent cancer cells and normal cells, respectively. Fig. 5a shows the survival rate of L-02 cells incubated with 200 μM of UIO-66-

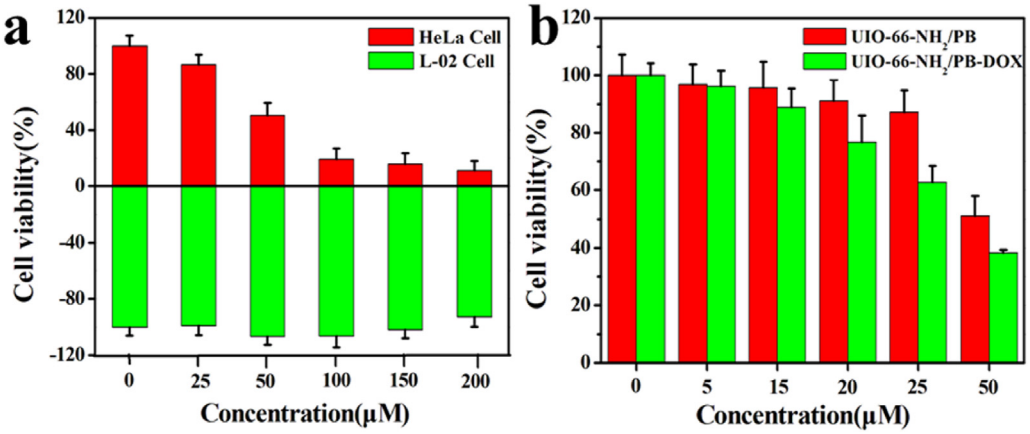

Fig. 5. a) Viability of HeLa cells and L-02 cell after 24 h of incubation with UIO-66-NH_2/PB; b)Cell viability of HeLa cells after 24 h of incubation of UIO-66-NH_2/PB and UIO-66-NH_2/PB-DOX. The error bar is the standard deviation of experimental data for three times.

NH_2/PB is still above 90%, indicating UIO-66-NH_2/PB is not harmful to normal cells. In comparison, the survival rate of HeLa cells is 50% incubated with only 50 μM of UIO-66-NH_2/PB, and the survival rate is 11% when the concentration of is 200 μM. It can be explained by that PB on the surface of UIO-66-NH_2 interact with H_2O_2 in tumor cells to produce ·OH to kill cancer cells. This indicates the selectivity of UIO-66-NH_2/PB and proves that the Fenton-like reaction of PB only occur in tumor cells. Therefore, UIO-66-NH_2/PB can be used as a satisfactory drug carrier, avoiding toxic and side effects on normal cells.

The cell viabilities of HeLa cells after incubation with different concentrations of UIO-66-NH_2/PB and DOX loaded UIO-66-NH_2/PB are compared, as shown in Fig. 5b. It can be seen that when the concentration of UIO-66-NH_2/PB increases to 50 μM, over 50% cancer cells are killed, indicating that sufficient hydroxyl radicals are by the Fenton-like reaction, killing more cancer cells. In comparison, UIO-66-NH_2/PB-DOX can kill more cancer cells than UIO-66-NH_2/PB. When the concentration of UIO-66-NH_2/PB-DOX increases to 50 μM, 62% cancer cells are killed. It demonstrates the synergetic effect of chemotherapy and chemo-dynamic therapy.

3.5. Fenton-like reaction analysis

In order to explore the Fenton like reaction of UIO-66-NH_2/PB in cancer cells environment, the dissolved oxygen amount produced in the reaction with H_2O_2 at pH 5.8 is tested, and the result is shown in Fig. 6a. It shows that when UIO-66-NH_2 is present alone, almost no O_2 is produced in H_2O_2, indicating UIO-66-NH_2 can't catalyzes H_2O_2 to produce O_2. In comparison, the produced O_2 increases with increasing reaction time when UIO-66-NH_2/PB is present in the H_2O_2 solution. It can be concluded that UIO-66-NH_2/PB can catalyze H_2O_2 into O_2 in cancer cells.

The generation of ·OH can be proved by using 3,3′,5,5′-tetramethylbenzidine (TMB), because ·OH can oxidize TMB and cause the solution to turn blue [40]. As showed in Fig. 6b, when UIO-66-NH_2/PB was added to H_2O_2, the color of the solution changed from colorless (solution 1) to green (solution 2). It can be explained that the generated ·OH can oxidize TMB, the solution changes from colorless to blue, and finally turns to yellow-green [41]. Furthermore, within 5 min NIR irradiation, the blue color becomes darker, as shown in Fig. 6c. It confirms that more hydroxyl radicals can be generated under NIR irradiation. In order to know whether H_2O can be catalyzed to produce ·OH, UIO-66-NH_2/PB was added to H_2O and TMB was used. The result was shown in Fig. S9. It is clear there is no obvious change of water color with or without NIR, indicating that water will not produce ·OH under these conditions. It confirms that ·OH can only be produced in TME, because of overexpressed H_2O_2. Therefore, UIO-66-NH_2/PB particles can catalyze the H_2O_2 of into hydroxyl radicals (·OH) and O_2 through Fenton-like reaction in TME, which can induce cell apoptosis [41] and increasing the oxygen concentration to improve hypoxia and reduce drug resistance [42].

3.6. In vivo T_2 MRI performance

To demonstrate the MRI contrast ability in vivo, 0.1 mL of UIO-66-NH_2/PB in PBS (5 mg/mL in PBS, 25 mg of per kilogram of mouse body weight) were injected into the mice via the tail vein. Fig. S10 shows the in vivo magnetic resonance imaging performance of UIO-66-NH_2/PB. As the time after injection is prolonged, the tumor site in mice changed from bright to dark and bright again. The time of the T_2 imaging contrast agent circulating in the body and the new metabolism in the mouse body will affect the intensity of the contrast agent imaging. It can be seen that the MRI-imaging intensity of the experimental group is significantly stronger than that of the control group. This shows that UIO-66-NH_2/PB can be used for live imaging as a T_2 -weighted MRI imaging agent.

3.7. In vivo antitumor activities

The synergistic therapeutic effect of chemotherapy, PTT and CDT of UIO-66-NH_2/PB in vivo is evaluated, and the result is shown in Fig. 7. Tumor-bearing mice were injected intravenously with UIO-66-NH_2/PB-DOX. After intravenous injection of different preparations, the tumor growth of mice is shown in Fig. 7a. Tumor growth in mice treated with UIO-66-NH_2/PB-DOX is significantly suppressed, which could be attributed to the synergetic effect of chemotherapy and CDT. Tumor of the mice treated with UIO-66-NH_2/PB-DOX and NIR reduces, indicating the better effect of synergetic therapy of chemotherapy, PTT and CDT. Changes in mice weight are shown in Fig. 7b. There is no significant change in body weight of mice during the entire comparative treatment process. The tumor change of mice treated with UIO-66-NH_2/PB + NIR is shown in Fig. 7c. It is clear that the tumor becomes small after 10 days treatment. Imaging of near-infrared light in mice is shown in Fig. 7d. It can not only prove the photo-thermal effect but also provide another method to obtain the information of tumor.

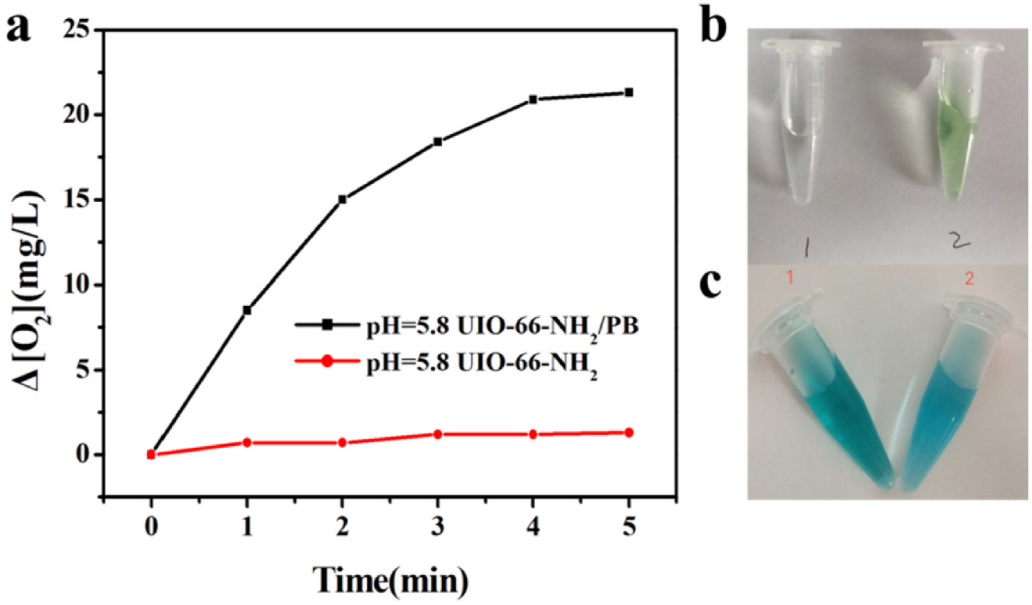

Fig. 6. a) UIO-66-NH_2/PB and UIO-66-NH_2 dissolved oxygen at pH = 5.8; b) Photo of TMB solution color change before and after adding UIO-66-NH_2/PB; c) Photograph of solution color change after adding UIO-66-NH_2/PB to TMB within 5 min NIR irradiation (c1) or without NIR(c2). (For interpretation of the references to color in this figure legend, the reader is referred to the Web version of this article.)

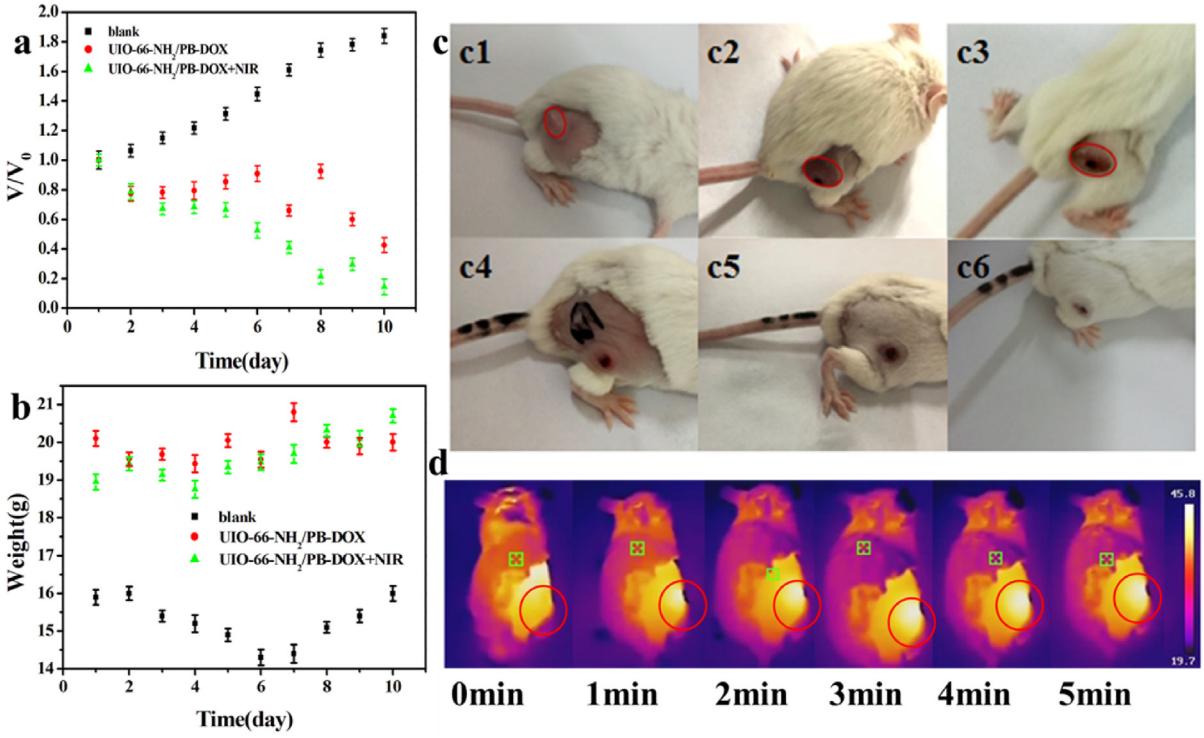

Fig. 7. a) Tumor growth curves of mice after intravenous injection with different formulations. Each dose of 150 μL PBS , 150 μL 0.50 mg/mL UIO-66-NH_2/PB and 150 μL 0.50 mg/mL UIO-66-NH_2/PB + NIR(5min); b) Body weight was recorded in vivo antitumor; c) Photographs of tumor changes of mice after the treatment. c1, c2, c3 are pictures of blank mice on days 2, 6 and 10; c4, c5, c6 are pictures of the treated mice on days 2, 6 and 10, respectively. d) In vivo near infrared light images mice after injection of UIO-66-NH_2/PB. Data were presented as mean ± sd (n = 3).

4. Conclusions

In summary, a novel hybrid material UIO-66-NH_2/PB was successfully synthesized. The PB particles are attached on the surface of UIO-66-NH_2 through the coordination between Fe ions of PB and amino groups of UIO-66-NH_2, thus forming UIO-66-NH_2/PB. It can be used as drug carrier for loading DOX through the hydrogen bonding, and release DOX in response to pH due to protonation in the acidic environment of the tumor. Due to the attached PB on the surface, UIO-66-NH_2/PB can be also used as a Fenton-like agent to

catalyze endogenous H_2O_2 in tumor cells into ·OH to kill more cancer cells, and produce oxygen at the same time to regulate hypoxia to improve the anticancer efficiency of released DOX. All in all, this comprehensive study has demonstrated that UIO-66-NH_2/PB is highly promising as a multifunctional drug carrier with high drug loading, pH-responsive, and MRI and infrared thermal imaging, cooperating with chemotherapy photo-thermal therapy and chemo-dynamic therapy, providing a new strategy for accurate cancer treatment in the near future.

Supporting information

In this supporting information, synthesis methods, drug loading and release, ICP analysis , MRI imaging, N_2 absorption−desorption isotherms, EDX elemental mapping of UIO-66-NH_2/PB, X-ray diffraction (XRD) patterns, FT-IR spectra and Heating curves of DOX loaded UIO-66-NH_2/PB, Mechanism of pH-responsive release of DOX, Drug release rate under near infrared light irradiation in pH 7.4, OH detection in water, T_2-weighted images and List of pH responsive drug carriers are introduced.

CRediT authorship contribution statement

Haiqing Gao: Data curation, Methodology, Writing - original draft. **Bin Chi:** Data curation, Methodology, Resources. **Feng Tian:** Supervision. **Mingyue Xu:** Software, Validation. **Zushun Xu:** Visualization, Investigation. **Ling Li:** Conceptualization, Methodology, Software, Writing - review & editing. **Jing Wang:** Methodology, Software, Resources.

Declaration of competing interest

The authors declare that they have no known competing financial interests or personal relationships that could have appeared to influence the work reported in this paper.

Acknowledgments

This work was supported by Ministry of Education Key Laboratory for the Synthesis and Application of Organic Function Molecules.

Appendix A. Supplementary data

Supplementary data to this article can be found online at https://doi.org/10.1016/j.jallcom.2020.157329.

References

[1] C.M. Oh, D. Lee, H.J. Kong, S. Lee, Y.J. Won, K.W. Jung, H. Cho, Causes of death among cancer patients in the era of cancer survivorship in Korea: attention to the suicide and cardiovascular mortality, Cancer medicine 9 (2020) 1741−1752, https://doi.org/10.1002/cam4.2813.

[2] D.D. Wang, H.H. Wu, W.Q. Lim, S.Z.F. Phua, P.P. Xu, Q.W. Chen, Z. Guo, Y.L. Zhao, A mesoporous nanoenzyme derived from metal−organic frameworks with endogenous oxygen generation to alleviate tumor hypoxia for significantly enhanced photodynamic therapy, Adv. Mater. 31 (2019) 1901893−1901901, https://doi.org/10.1002/adma.201901893.

[3] S.T. Gao, Y. Jin, K. Ge, Z.H. Li, H.F. Liu, X.Y. Dai, Y.H. Zhang, S.Z. Chen, X.J. Liang, J.C. Zhang, Self-supply of O_2 and H_2O_2 by a nanocatalytic medicine to enhance combined chemo/chemodynamic therapy, Adv. Sci. 6 (2019) 1902137−1902145, https://doi.org/10.1002/advs.201902137.

[4] D.D. Wang, J.J. Zhou, R.H. Chen, R.H. Shi, G.Z. Zhao, G.L. Xia, R. Li, Z.B. Liu, J. Tian, H.J. Wang, Z. Guo, H.B. Wang, Q.W. Chen, Controllable synthesis of dual-MOFs nanostructures for pH-responsive artemisinin delivery, magnetic resonance and optical dual-model imaging-guided chemo/photothermal combinational cancer therapy, Biomaterials 100 (2016) 27−40, https://doi.org/10.1016/j.biomaterials.2016.05.027.

[5] Y.J. Cheng, J.J. Hu, S.Y. Qin, A.Q. Zhang, X.Z. Zhang, Recent advances in functional mesoporous silica-based nanoplatforms for combinational photochemotherapy of cancer, Biomaterials 232 (2020) 119738−119805, https://doi.org/10.1016/j.biomaterials.2019.119738.

[6] W. Cai, J.Q. Wang, C.C. Chu, W. Chen, C.S. Wu, G. Liu, Metal−organic framework-based stimuli-responsive systems for drug delivery, Adv. Sci. 6 (2019) 1801526−1801545, https://doi.org/10.1002/advs.201801526.

[7] S.Y. Teresa, M. Angelika, C. Patrick, S. Christian, Nanoparticles of metal-organic frameworks: on the road to in vivo efficacy in biomedicine, Adv. Mater. 30 (2018) 1707365−1707379, https://doi.org/10.1002/adma.201707365.

[8] X.Q. Qian, X.X. Han, L.D. Yu, T.M. Xu, Y. Chen, Manganese-based functional nanoplatforms: nanosynthetic construction, physiochemical property, and theranostic applicability, Adv. Funct. Mater. 30 (2019) 1907066−1907105, https://doi.org/10.1002/adfm.201907066.

[9] Z. Wang, S.G. Hu, J. Yang, A. Liang, Y. Li, Q. Zhuang, J. Gu, Nanoscale Zr-based MOFs with tailorable size and introduced mesopore for protein delivery, Adv. Funct. Mater. 28 (2018) 1707356−1707364, https://doi.org/10.1002/adfm.201707356.

[10] R. Freund, U. Lächelt, T. Gruber, B. Rühle, S. Wuttke, Multifunctional efficiency: extending the concept of atom economy to functional nanomaterials, ACS Nano 12 (2018) 2094−2105. http://doi: 10.1021/acsnano.8b00932.

[11] S. Wuttke, A. Zimpel, T. Bein, S. Braig, K. Stoiber, A. Vollmar, D. Müller, K. Haastert-Talini, J. Schaeske, M. Stiesch, G. Zahn, A. Mohmeyer, P. Behrens, O. Eickelberg, D.A. Bölükbas, S. Meiners, Validating metal-organic framework nanoparticles for their nanosafety in diverse biomedical applications, Adv. Healthcare Mater. 6 (2017) 1600818−1600828, https://doi.org/10.1002/adhm.201600818.

[12] M.X. Wu, Y.W. Yang, Metal-organic framework (MOF)-based drug/cargo delivery and cancer therapy, Adv. Mater. 29 (2017) 1606134−1606153, https://doi.org/10.1002/adma.201606134.

[13] W.X. Lin, Q. Hu, K. Jiang, Y.Y. Yang, Y. Yang, Y.J. Cui, G.D. Qian, A porphyrin-based metal−organic framework as a pH-responsive drug carrier, J. Solid State Chem. 237 (2016) 307−312, https://doi.org/10.1016/j.jssc.2016.02.040.

[14] M. Kotzabasaki, G.E. Froudakis, Review of computer simulations on anticancer drug delivery in MOFs, Inorg. Chem. Front. 5 (2018) 1255−1272, https://doi.org/10.1039/C7QI00645D.

[15] Z.Q. Shi, X.R. Chen, L. Zhang, S.P. Ding, X. Wang, Q.F. Lei, W.J. Fang, FA-PEG decorated MOF nanoparticles as targeted drug delivery system for controlled release of autophagy inhibitor, Biomater. Sci. 6 (2018) 2582−2590, https://doi.org/10.1039/C8BM00625C.

[16] W. Zhu, W.Q. Huang, L.P. Ye, Y.H. Deng, Q.L. Xie, Y.B. Jiang, Facile preparation of succinylated-zein-ZIF-8 hybrid for enhanced stability and pH-responsive drug delivery, Chem. Eng. 228 (2020) 115981−116000, https://doi.org/10.1016/j.ces.2020.115981.

[17] J. Schnabel, R. Ettlinger, H. Bunzen, Zn-MOF-74 as pH-responsive drug delivery system of arsenic trioxide, ChemNanoMat 6 (2020) 1229−1236, https://doi.org/10.1002/cnma.202000221.

[18] A.R. Chowdhuri, D. Laha, S. Chandra, P. Karmakar, S.K. Sahu, Synthesis of multifunctional upconversion NMOFs for targeted antitumor drug delivery and imaging in triple negative breast cancer cells, Chem. Eng. J. 319 (2017) 200−211, https://doi.org/10.1016/j.cej.2017.03.008.

[19] S.S. Gao, H. Lin, H.X. Zhang, H.L. Yao, Y. Chen, J.L. Shi, Nanocatalytic tumor therapy by biomimetic dual inorganic nanozyme-catalyzed cascade reaction, Adv. Sci. 6 (2019) 1801733−1801744, https://doi.org/10.1002/advs.201801733.

[20] H. Zhang, L. Sun, X. Xiao, R.G. Xie, C.H. Liu, Y.F. Wang, Y.L. Wei, H.B. Zhang, L.L. Liu, Krüppel-like factor 8 contributes to hypoxia-induced MDR in gastric cancer cells, Canc. Sci. 105 (2014) 1109−1115, https://doi.org/10.1111/cas.12483.

[21] M.Z. Zou, W.L. Liu, C.X. Li, D.W. Zheng, J.Y. Zeng, F. Gao, J.J. Ye, X.Z. Zhang, A multifunctional biomimetic nanoplatform for relieving hypoxia to enhance chemotherapy and inhibit the PD-1/PD-L1 axis, Small 14 (2018) 1801120−1801130, https://doi.org/10.1002/smll.201801120.

[22] S.S. Li, L. Shang, B.L. Xu, S.H. Wang, K. Gu, Q.Y. Wu, Y. Sun, Q.H. Zhang, H.L. Yang, F.R. Zhang, L. Gu, T.R. Zhang, H.Y. Liu, A nanozyme with photo-enhanced dual enzyme-like activities for deep pancreatic cancer therapy, Angew. Chem. 58 (2019) 12624−12631, https://doi.org/10.1002/anie.201904751.

[23] B.W. Yang, Y. Chen, J.L. Shi, Nanocatalytic medicine, Adv.Mater. 31 (2019) 1901778−1901832, https://doi.org/10.1002/adma.201901778.

[24] L.S. Lin, J.B. Song, L. Song, K.M. Ke, Y.J. Liu, Z.J. Zhou, Z.Y. Shen, J. Li, Z. Yang, W. Tang, G. Niu, H.H. Yang, X.Y. Chen, Simultaneous fenton-like ion delivery and glutathione depletion by MnO_2-based nanoagent enhances chemodynamic therapy, Angew. Chem. 130 (2018) 4996−5000, https://doi.org/10.1002/ange.201712027.

[25] T.T. Wang, H. Zhang, H.H. Liu, Q. Yuan, F. Ren, Y.B. Han, Q. Sun, Z. Li, M.Y. Gao, Boosting H_2O_2-guided chemodynamic therapy of cancer by enhancing reaction kinetics through versatile biomimetic fenton nanocatalystsand the second near-infrared light irradiation, Adv. Funct. Mater. 30 (2019) 1906128−1906142, https://doi.org/10.1002/adfm.201906128.

[26] Z.G. Qin, Y. Li, N. Gu, Progress in applications of prussian blue nanoparticles in biomedicine, Adv. Healthcare Mater. 7 (2018) 1800347−1800359, https://doi.org/10.1002/adhm.201800347.

[27] B. Kong, C. Selomulya, G.F. Zheng, D.Y. Zhao, New faces of porous Prussian blue: interfacial assembly of integrated hetero-structures for sensing applications, Chem. Soc. Rev. 44 (2015) 7997−8018, https://doi.org/10.1039/C5CS00397K.

[28] D.D. Wang, J.J. Zhou, R.H. Shi, H.H. Wu, R.H. Chen, B.C. Duan, G.L. Xia, P.P. Xu, H. Wang, S. Zhou, C.M. Wang, H.B. Wang, Z. Guo, Q.W. Chen, Biodegradable core-shell dual-metal-organic frameworks nanotheranostic agent for multiple imaging guided combination cancer therapy, Theranostics 7 (2017) 4605–4617, https://doi.org/10.7150/thno.20363.

[29] D. Yang, G. Yang, S. Gai, F. He, G. An, Y. Dai, R. Lv, P. Yang, Au25 cluster functionalized metal-organic nanostructures for magnetically targeted photodynamic/photothermal therapy triggered by single wavelength 808 nm near-infrared light, Nanoscale 7 (2017) 19568–19578, https://doi.org/10.1039/C5NR06192J.

[30] X. Qu, A. Allan, G. Chui, T.J. Hutchings, P. Jiao, L. Johnson, W.Y. Leung, P.K. Li, G.R. Steel, A.S. Thompson, M.D. Threadgill, T.J. Woodman, M.D. Lloyd, Hydrolysis of ibuprofenoyl-CoA and other 2-APA-CoA esters by human acyl-CoA thioesterases-1 and -2 and their possible role in the chiral inversion of profens, Biochem. Pharmacol. 86 (2013) 1621–1625, https://doi.org/10.1016/j.bcp.2013.08.067.

[31] S. Sahu, S. Mohapatra, Multifunctional magnetic fluorescent hybrid nanoparticles as carriers for the hydrophobic anticancer drug 5-fluorouracil, Dalton Trans. 42 (2013) 2224–2231, https://doi.org/10.1039/C2DT31812A.

[32] L. Zhou, W. Wang, S.H. Wei, Y.Y. Feng, J.H. Zhou, J.H. Liu, J. Shen, Encapsulation of hydrophobic anticancer drug in nano-scale porous ceramic materials for photodynamic therapy, J. Porous Mater. 18 (2011) 517–522, https://doi.org/10.1007/s10934-010-9405-1.

[33] M. Pyrasch, B. Tieke, Electro-and photoresponsive films of prussian blue prepared upon multiple sequential adsorption, Langmuir 17 (2001) 7706–7709, https://doi.org/10.1021/la0104424.

[34] K. Itaya, I. Uchida, Nature of intervalence charge-transfer bands in Prussian blues, Inorg. Chem. 25 (1986) 389–392, https://doi.org/10.1021/ic00223a034.

[35] M.C. Li, W.F.J. Whitmore, R. Golbey, H. Grabstald, Effects of combined drug therapy on metastatic cancer of the testis, J. Am. Med. Assoc. 174 (1960) 1291–1299, https://doi.org/10.1001/jama.1960.03030100059013.

[36] S.X. Bao, J.Y. Li, B.Y. Guan, M.J. Jia, O. Terasaki, J.H. Yu, A green selective water-etching approach to MOF@Mesoporous SiO_2 Yolk-Shell nanoreactors with enhanced catalytic stabilities, Matter 3 (2020) 498–508, https://doi.org/10.1016/j.matt.2020.06.021.

[37] P.C. Lemaire, D.T. Lee, J.J. Zhao, G.N. Parsons, Reversible low-temperature metal node distortion during atomic layer deposition of Al_2O_3 and TiO_2 on UiO-66-NH_2 metal-organic framework crystal surfaces, ACS Appl. Mater. Interfaces 9 (2017) 22042–22054, https://doi.org/10.1021/acsami.7b05214.

[38] J.H. Santos, M.T.J. Quimque, A.P.G. Macabeo, M.J.T. Corpuz, Y.M. Wang, T.T. Lu, C.H. Lin, O.B. Villaflores, Enhanced oral bioavailability of the pharmacologically active lignin magnolol via Zr-Based metal organic framework impregnation, Pharmaceutics 12 (2020), https://doi.org/10.3390/pharmaceutics12050437, 437-434.

[39] M.J.S. Langman, K.K. Cheng, E.A. Gilman, R.J. Lancashire, Effect of anti-inflammatory drugs on overall risk of common cancer: case-control study in general practice research database, BMJ 320 (2000) 1642–1646, https://doi.org/10.1136/bmj.320.7250.1642.

[40] H. Ranji-Burachaloo, F. Karimi, K. Xie, Q. Fu, P.A. Gurr, D.E. Dunstan, G.G. Qiao, MOF-mediated destruction of cancer using the cell's own hydrogen peroxide, ACS Appl. Mater. Interfaces 9 (2017) 33599–33608, https://doi.org/10.1021/acsami.7b07981.

[41] X. Sun, G.L. Zhang, R.H. Du, R. Xu, D.W. Zhu, J.C. Qian, G. Bai, C. Yang, Z.Y. Zhang, X. Zhang, D.H. Zou, Z.Y. Wu, A biodegradable MnSiO3@Fe3O4 nanoplatform for dual-mode magnetic resonance imaging guided combinatorial cancer therapy, Biomaterials 194 (2019) 151–160, https://doi.org/10.1016/j.biomaterials.2018.12.004.

[42] S.Q. Liu, S. Cheng, L.R. Feng, X.M. Wang, Z.G. Chen, J. Hazard, Effect of alkali cations on heterogeneous photo-fenton process mediated by Prussian blue colloids, J. Hazard Mater. 182 (2010) 665–671, https://doi.org/10.1016/j.jhazmat.2010.06.083.